Journal of Colloid and Interface Science 724 (2026) 141247

Contents lists available at ScienceDirect

Journal of Colloid And Interface Science

journal homepage: www.elsevier.com/locate/jcis

Fluorinated ionic molecule enables synergistic surface passivation and charge balancing for efficient green perovskite quantum-dot light-emitting diodes

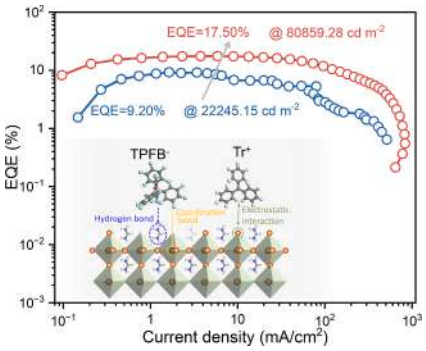
Di Shen [a], Jianhao Ding [a], Yuhang Tan [a], Yujie Wen [a], Xinning Wang [a], Xiankan Zeng [a], Maolin Mu [a], Chenglong Li [a], Jingjing Cao [c], Xiaoqiang Fan [a], Weiqing Yang [a,b], Wen Li [a,*]

[a] Key Laboratory of Advanced Technologies of Materials (Ministry of Education), School of Materials Science and Engineering, Southwest Jiaotong University, Chengdu 610031, PR China
[b] Research Institute of Frontier Science, Southwest Jiaotong University, Chengdu 610031, PR China
[c] School of Environmental Science and Engineering, Shanghai Jiao Tong University, Shanghai, 200240, PR China

HIGHLIGHTS

- TrTPFB is successfully introduced as a fluorinated ionic molecule into $FAPbBr_3$ PeQDs.
- Multi-site interactions stabilize the PeQD surface and suppress nonradiative recombination.
- TrTPFB induces p-type modulation, reducing interfacial charge accumulation.
- Threefold enhancement in T_{50} lifetime highlights improved device stability.

GRAPHICAL ABSTRACT



ARTICLE INFO

Keywords:
Perovskite quantum dots
Surface passivation
P-type electronic modulation
Charge balance
Stability

ABSTRACT

Perovskite quantum-dot light-emitting diodes (PeQLEDs) remain limited by coupled surface and interfacial losses: labile ligand binding produces trap-rich perovskite quantum dot (PeQD) surfaces while unbalanced carrier injection accelerates interfacial charge accumulation and nonradiative recombination. Here, triphenylmethylium tetrakis(pentafluorophenyl)borate (TrTPFB) is introduced as a fluorinated ionic molecule to synergistically regulate both the surface coordination and charge-injection behavior of $FAPbBr_3$ PeQDs. Density functional theory (DFT) calculations reveal pronounced charge redistribution between TrTPFB and the PeQD surface. Experimental results show that the fluorinated tetrakis(pentafluorophenyl)borate ($TPFB^-$) anion and the positively charged triphenylmethylium (Tr^+) cation cooperatively stabilize the surface coordination environment and suppress trap-mediated nonradiative recombination. TrTPFB also induces p-type electronic modulation of the PeQD film, shifts the Fermi level toward the valence band, lowers the hole-injection barrier, and mitigates interfacial charge accumulation. Consequently, The combined operation of these mechanisms significantly improves the photoluminescence quantum yield (PLQY) of perovskite films to an impressive 98.50%. The

* Corresponding author.
E-mail address: liwen3337@swjtu.edu.cn (W. Li).

https://doi.org/10.1016/j.jcis.2026.141247
Received 10 June 2026; Received in revised form 27 July 2026; Accepted 28 July 2026
Available online 29 July 2026
0021-9797/© 2026 Elsevier Inc. All rights are reserved, including those for text and data mining, AI training, and similar technologies.

corresponding green PeQLED achieves a peak external quantum efficiency of 17.50%, a maximum luminance of 80,859.28 cd m^{-2}, and an approximately threefold increase in the average T_{50} lifetime compared with the control device. This work establishes a fluorinated ionic molecular strategy that integrates surface passivation and charge-injection regulation for efficient and stable PeQLEDs.

1. Introduction

Metal halide perovskite quantum dots (PeQDs) have emerged as highly promising emissive materials for next-generation displays and lighting technologies because of their tunable bandgaps, narrow emission linewidths, high color purity, strong defect tolerance, and solution processability [1–6]. Despite rapid progress in perovskite quantum-dot light-emitting diodes (PeQLEDs), their further development is still limited by coupled losses at the PeQD surfaces and device interfaces. The soft ionic lattice and dynamic ligand-binding of PeQDs render their surfaces susceptible to ligand desorption, undercoordinated ionic defects, and structural disorder during purification, film formation, and device operation [7,8]. These surface imperfections not only promote trap-assisted nonradiative recombination but also disrupt carrier injection and recombination within the emissive layer, thereby reducing device efficiency and poor operational stability [9–14].

Conventional PeQDs typically employ long-chain organic ligands such as oleic acid (OA) and oleylamine (OAm) to regulate crystal growth and maintain colloidal stability. However, OA/OAm binding to PeQD surface is dynamically reversible, making ligand desorption prone to occur during purification and film formation, exposing undercoordinated Pb^{2+} and halide-related defects. These defects serve as carrier-trapping and nonradiative recombination centers, thereby suppressing radiative recombination efficiency [15–17]. In addition, the insulating alkyl chains increase the interdot spacing and weaken electronic coupling between adjacent PeQDs, thereby impeding charge injection and transport within the emissive layer [15,18,19]. Therefore, simultaneously stabilizing the PeQD surface and improving charge transport is essential for achieving efficient and stable PeQLEDs.

Extensive ligand-engineering strategies have been developed to address these limitations [20,21]. Lewis-base or Lewis-acidic molecules, including sulfonate, carboxylate, and amine-containing ligands, can coordinate with undercoordinated ionic sites and suppress defect-assisted recombination [22–24]. Short-chain or conjugated ligands can partially replace insulating native ligands, decrease interdot spacing, and stengthen electronic coupling [25–27]. Bifunctional and multidentate ligands have also been used to reinforce surface binding and improve structural stability [28–30]. Nevertheless, many reported approaches primarily address either defect passivation or charge transport [31,32]. Molecular strategies that can integrate surface-defect passivation, energy-level regulation, and carrier-injection balance remain highly desirable.

Herein, we introduce triphenylmethylium tetrakis(pentafluorophenyl)borate (TrTPFB) is introduced as a fluorinated ionic molecule to co-regulate the surface chemistry and electronic properties of $FAPbBr_3$ PeQDs. Negatively polarized fluorine atoms in the tetrakis (pentafluorophenyl)borate ($TPFB^-$) coordinate with undercoordinated Pb^{2+} sites and form N-H···F hydrogen bonds with FA^+, while the triphenylmethylium (Tr^+) cation electrostatically interacts with surface Br^-. These multi-site interactions stabilize the surface coordination environment, suppress trap-mediated nonradiative recombination, and improve the optical stability of the PeQDs. Meanwhile, TrTPFB-modified PeQD emissive layer exhibits enhanced hole transport owing to the p-type modulation induced by the electron-withdrawing fluorinated aryl groups, the reduced hole-injection barrier, and the suppressed interfacial charge accumulation. Through this coupled surface and electronic regulation, the optimized device achieves a peak external quantum efficiency (EQE) of 17.50%, a maximum luminance of 80,859.28 cd m^{-2}, and an approximately threefold longer average T_{50} lifetime than the control device. This work highlights fluorinated ionic molecular regulation as an effective route to efficient and stable PeQLEDs.

2. Results and discussion

$FAPbBr_3$ QDs were synthesized using a modified ligand-assisted recrystallization method based on previous reports [33–36]. TrTPFB consists of triphenylmethyl cations[$(C(C_6H_5)_3)^+$, Tr^+] and tetra-(pentafluorophenyl) borate anions [$(B(C_6F_5)_4)^-$, $TPFB^-$], with its molecular structure displayed in **Fig. S1**. TrTPFB has been employed as an effective p-type dopant in organic semiconductors, where its strong electron-withdrawing characteristics can modulate the electronic structure and carrier distribution. However, its application in metal halide perovskite materials remains largely unexplored [37,38]. To probe the underlying interaction mechanisms, density functional theory (DFT) calculations were performed. As shown in Fig. 1a, electrostatic potential (ESP) shows that the electron distribution is highly polarized, significant electron localization is observed on the fluorine atoms with high electronegativity. Such charge localization implies that the electron-rich fluorine atoms can serve as potential coordination sites for uncoordinated ion defects on the perovskite surface. To simplify the theoretical model, dissociated the anions ($TPFB^-$) and cations (Tr^+) of TrTPFB were separately positioned at representative surface sites for structural optimization, and charge density difference plots were generated to intuitively visualize the electronic interactions between these ionic species and the $FAPbBr_3$ QD surface (Fig. 1b, **Fig. S2**). The yellow regions represent charge accumulation, while green regions denote charge depletion. On the basis of these calculations, three major interaction modes between TrTPFB and the perovskite surface are identified (Fig. 1c). First, the fluorine atoms in the $TPFB^-$ anion coordinate with uncoordinated lead sites, yielding an interaction energy of 0.251 eV. Second, the fluorine atoms tend to form hydrogen bonds with the $-NH_2$ groups in FA^+ cations, accompanied by significant electron density transfer from the perovskite surface to the $TPFB^-$, giving a strong interaction energy of 2.592 eV. Third, the positively charged Tr^+ interacts with surface halide anions through electrostatic attraction, effectively anchoring the highly mobile halide ions, with the electron migrating from the benzene rings of the Tr^+ cation to the perovskite surface and an interaction energy of 0.284 eV (**Table S1**). Collectively, these calculations suggest that TrTPFB can stabilize the local coordination environment of the PeQD surface through multiple ionic and coordination interactions, which is expected to suppress surface-defect formation and reduce ion-related instability.

To verify the proposed interaction mechanisms, nuclear magnetic resonance (NMR) spectroscopy was employed to investigate the interaction between TrTPFB and the perovskite precursor solution (Fig. 1d). For the FABr-only sample, the resonance signal in DMSO-d_6 solvent appeared at approximately 8.7 ppm, corresponding to the acidic protons of the FA^+ cations. Upon addition of TrTPFB, this signal moved significantly downfield to 9.022 ppm, indicating the formation of N—H···F hydrogen bond between $-NH_2$ $^+$ proton of FA^+ and fluorine atoms of $TPFB^-$. The high electronegativity of the fluorine atom significantly reduces the proton electron cloud density, thereby stabilizing the ligand on the perovskite surface and suppressing ligand desorption. Additionally, multiple peaks observed between 7.15 and 7.25 ppm are attributed to the aromatic protons of the triphenylmethyl (Tr^+) cation (typically 6.5–8.0 ppm). The successful incorporation of TrTPFB into the perovskite surface was further confirmed by X-ray photoelectron spectroscopy (XPS), as evidenced by the detection of the F 1 s signal in the target

sample (Fig. 1e, f, **and S3**). Compared to the control, the Pb $4f_{5/2}$ and Pb $4f_{7/2}$ peaks of the target sample shift to lower binding energies, suggesting coordination of $TPFB^-$ anions with undercoordinated Pb^{2+} sites. Similarly, the Br 3d signal also shifts to lower binding energy, which can be attributed to the electrostatic interaction between the positively charged Tr^+ cations and Br^- anions in the perovskite lattice. This interaction increases the electron cloud density around the bromine atoms and subsequently decreases their binding energy. Collectively, these spectroscopic results verify the multi-site interaction between TrTPFB and the PeQD surface, thereby supporting the proposed surface-passivation mechanism.

The surface morphology of the PeQD films was characterized using scanning electron microscopy (SEM), as shown in **Fig. S4**. The control film exhibited distinct grains with varied sizes, often associated with residual and unreacted lead halide species [39]. In contrast, the TrTPFB-modified film presented a smooth and uniform surface without large particle aggregates. This improved uniformity was further supported by energy-dispersive X-ray spectroscopy (EDS) mapping (**Fig. S5**). The uniform distribution of fluorine (F) element across the target film confirmed the successful and homogeneous incorporation of TrTPFB. Transmission electron microscopy (TEM) was further employed to directly examine the morphology and size distribution of the as-prepared PeQDs (**Fig. S6**). Representative enlarged TEM images of PeQDs are presented in Fig. 2a. The control PeQDs exhibited a relatively broad particle-size distribution with an average grain size of 10.01 nm. In comparison, the target PeQDs modified by TrTPFB displayed well-defined grain boundaries and a significantly narrower size distribution, with the average grain size reduced to 9.30 nm. These results indicate that the incorporation of TrTPFB effectively regulates the growth behavior of PeQDs and optimizes their morphological uniformity. To further investigate the crystallographic properties and phase purity of the films, X-ray diffraction (XRD) analysis was performed (**Fig. S7**). Compared with the control, no impurity peaks appeared after TrTPFB modification, while the diffraction peak intensity was significantly increased, demonstrating that TrTPFB incorporation not only preserves but also enhances the crystallinity of the QDs.

Such structural and morphological improvements are expected to positively promote the photoluminescence properties of PeQDs [40,41]. Fig. 2a presents the ultraviolet-visible (UV–vis) absorption and photoluminescence (PL) spectra of the prepared samples, revealing that TrTPFB-modified PeQDs exhibit prominently enhanced absorption and PL intensity relative to the control. To quantitatively evaluate the luminescence efficiency, the absolute photoluminescence quantum yields (PLQYs) of the films were measured. The target perovskite thin film exhibits a significantly improved PLQY, achieving a maximum value of 98.50%. The improvement of PLQY from an average of 49.71 ± 6.73% in the control perovskite film to 91.72 ± 5.18% after treatment suggests a noticeable reduction of non-radiative recombination (**Fig. S8 and Table S2**). To understand the origin of the enhanced PLQY, the defect-related electronic disorder of the PeQD films was first evaluated by Urbach energy analysis. The Urbach energy (E_U) was further calculated by fitting the correlation between absorption coefficient and photon energy. The lower E_U values indicate fewer defects [42]. The Urbach energy (E_U) was determined using the following relationship:

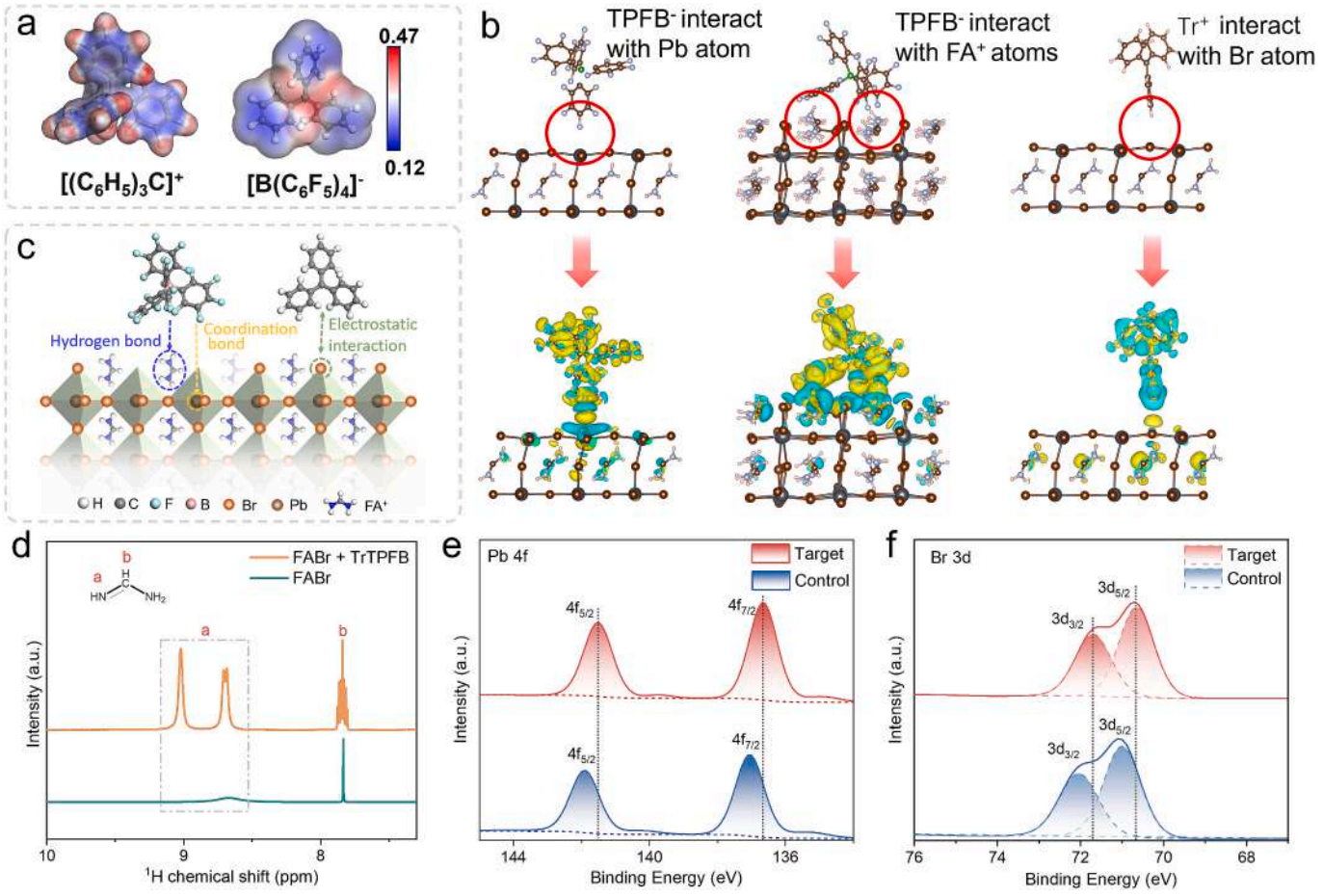


Fig. 1. The interaction mechanism between TrTPFB and $FAPbBr_3$ QDs. a) Simulated electrostatic potential (ESP) profiles of the TrTPFB molecule. b) Schematic illustration of the binding and passivation mechanism of TrTPFB on $FAPbBr_3$ QDs. c) Density functional theory (DFT) calculation models and charge-density-difference Plots of TrTPFB Interactions with the Perovskite (100) Surface. d) ^1H NMR spectra of pure FABr and the mixture of FABr with TrTPFB. XPS spectra of e) Pb 4f and f) Br 3d.

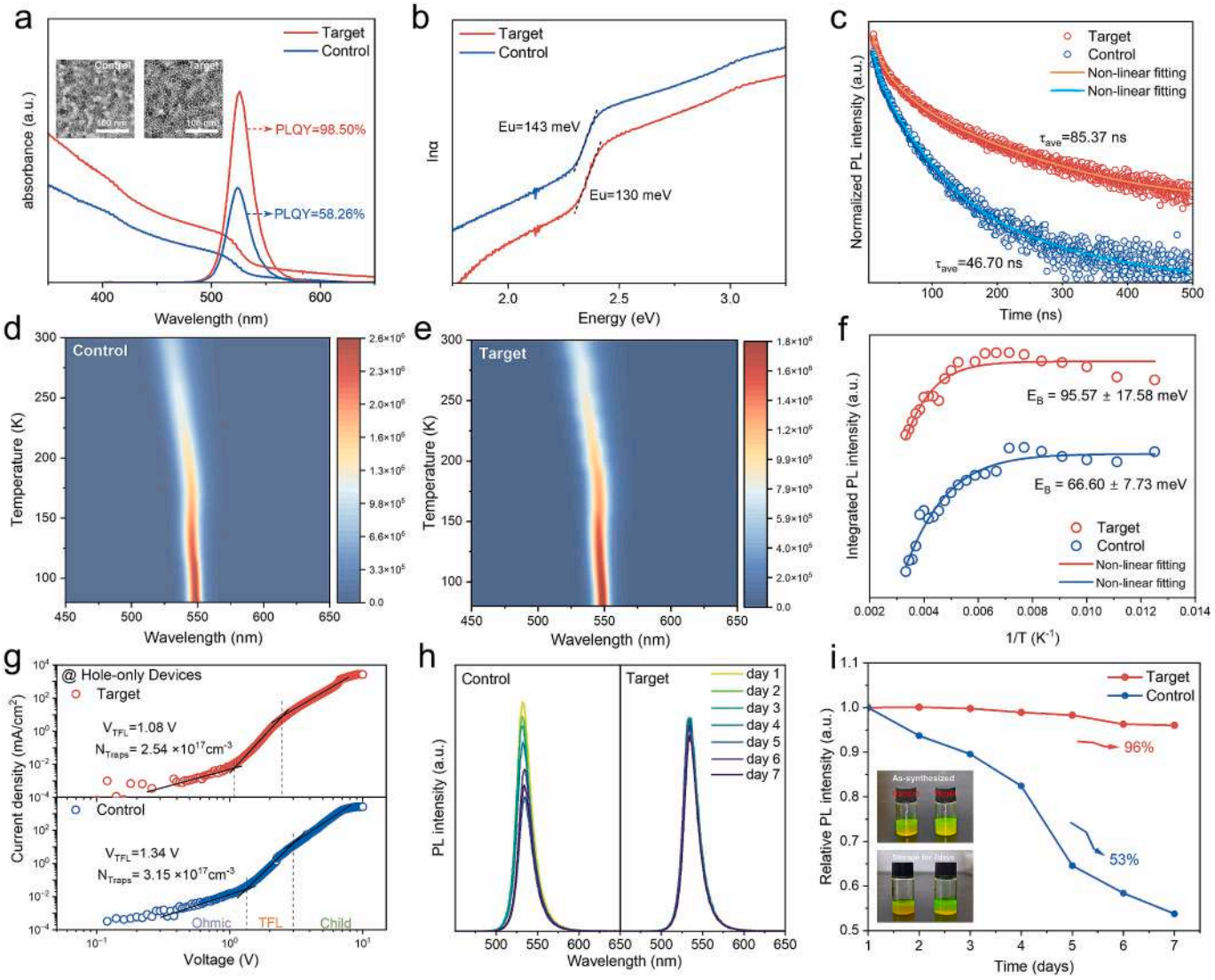


Fig. 2. Optical properties of PeQD films. a) Ultraviolet–visible (UV − vis) and steady-state PL spectra with the absolute PLQY values (Inset: representative TEM images of PeQD films). b) Urbach energy diagram. c) Time-resolved photoluminescence (TRPL) spectra. d and e) Two-dimensional (2D) temperature-dependent PL spectra. f) Integrated PL intensity as a function of reciprocal temperature (1000/T) for the calculation of exciton binding energy (E_B). g) Current density − voltage curves for the hole-only devices. h) PL stability of the PeQDs storage for different days. i) Evolution of the PL intensity for the QD solution samples stored over various durations (Inset: photographs of the as-synthesized and seven days stored samples under UV light).

$$\alpha(E) = \alpha_0 \exp\left[\sigma(T)\frac{E - E_0}{k_B T}\right]$$

where α(E) is the absorption coefficient; E_0 and α_0 are material parameters; σ(T) is the steepness parameter; k_B is the Boltzmann constant; and T is the temperature. As shown in Fig. 2b, the E_U value decreased from 143 meV for the control film to 130 meV after TrTPFB modification, demonstrating that the incorporation of TrTPFB effectively reduces defect-induced electronic disorder and suppresses the formation of localized trap states. The reduction of defect-related recombination was further confirmed by time-resolved photoluminescence (TRPL) measurements [43] (Fig. 2c). Compared with the control film, the TrTPFB-modified film exhibits a significantly prolonged average PL lifetime, increasing from 46.70 to 85.37 ns. To quantitatively evaluate the recombination kinetics, the radiative decay rate (k_r) and nonradiative decay rate (k_{nr}) were calculated based on the PLQY and average PL lifetime (τ_{avg}), with the results summarized in **Table S3**. The introduction of TrTPFB significantly reduced k_{nr} value, while the k_{nr} remains within the same order of magnitude. These results indicate that the enhanced PLQY mainly originates from the effective suppression of trap-mediated nonradiative recombination rather than accelerated radiative decay [19]. Therefore, the synergistic coordination interactions between TrTPFB and the PeQD surface effectively promote highly efficient radiative emission.

The nonradiative recombination process in perovskite films is governed by both defect-assisted trapping and the intrinsic exciton-phonon interaction [44]. Temperature-dependent PL measurements were performed from 80 to 300 K. The corresponding 2D and integrated PL intensity analysis are displayed in Fig. 2d-f, while the normalized one-dimensional (1D) and three-dimensional (3D) PL spectra are provided in **Fig. S9**. The thermal quenching effect in the target film is markedly suppressed compared to the control, demonstrating the effectiveness of TrTPFB in suppressing thermal quenching dominated by nonradiative recombination [45]. The extracted full width at half maximum (FWHM) curve from the 2D temperature-dependent PL graph (**Fig. S10**) shows excellent consistency between the experimental data and the theoretical fitting results ($R_2 > 0.99$). As summarized in **Table S4**, the target QDs possess a lower intrinsic broadening value (Γ_{inh}), indicating greatly

improved crystallization quality and uniformity after TrTPFB-modification [44,46–49]. The optimized film effectively alleviates exciton-phonon coupling within the emission layer (EML), thereby enhancing carrier mobility [50,51]. The exciton binding energy (E_B) was obtained by fitting the temperature-dependent integrated PL intensity based on the Arrhenius equation:

$$I(T) = \frac{I_0}{1 + Ae^{-E_B/k_BT}}$$

where I_0 is the PL intensity at 0 K; A is the pre-exponential coefficient; and k_B is the Boltzmann constant. E_B is defined as the energy required to dissociate an exciton into free charge carriers. A larger E_B indicates a higher potential barrier for exciton dissociation within the perovskite film [52]. The E_B of the target film was 95.57 me V, significantly higher than that of the control film at 66.60 me V. This substantial increase indicates that the TrTPFB molecules effectively inhibit the thermal dissociation of photogenerated electron-hole pairs at room temperature and prolong the exciton lifetime.

Space-charge-limited current (SCLC) measurements were further performed to quantitatively verify the defect passivation effect of TrTPFB. Single-carrier hole-only devices were fabricated with the structure of ITO/PEDOT:PSS/PVK/PeQDs/MoO_3/Ag, and their current density-voltage (J-V) characteristics were measured to determine the trap-state density (N_t) within the perovskite films (Fig. 2g). The trap density (N_t) is directly proportional to trap-filled-limit voltage (V_{TFL}) and can be quantitatively determined using the following formula [53]:

$$n_t = \frac{2\varepsilon\varepsilon_0 V_{TFL}}{eL^2}$$

V_{TFL} is the trap-filled limiting voltage deduced from the J-V curves; e is the elementary charge; and ε_0 and ε are the vacuum permittivity and relative permittivity, respectively. L is the thickness of the film (determined from the SEM cross-section in **Fig. S11**). The V_{TFL} of the hole-only device decreased from 1.34 V to 1.08 V upon the introduction of TrTPFB, and the corresponding N_t reduced from 3.15×10^{17} cm^{-3} to 2.54×10^{17} cm^{-3}. The reduced trap density indicates that TrTPFB effectively decreases electrically active trap states in the PeQD film, which is consistent with the suppressed nonradiative recombination revealed by PL analyses. Furthermore, the hole mobility (μ_h) was derived using the Mott-Gurney law in the trap-free Child's region [54]:

$$\mu_h = 8L^3J/9\varepsilon\varepsilon_0V^2$$

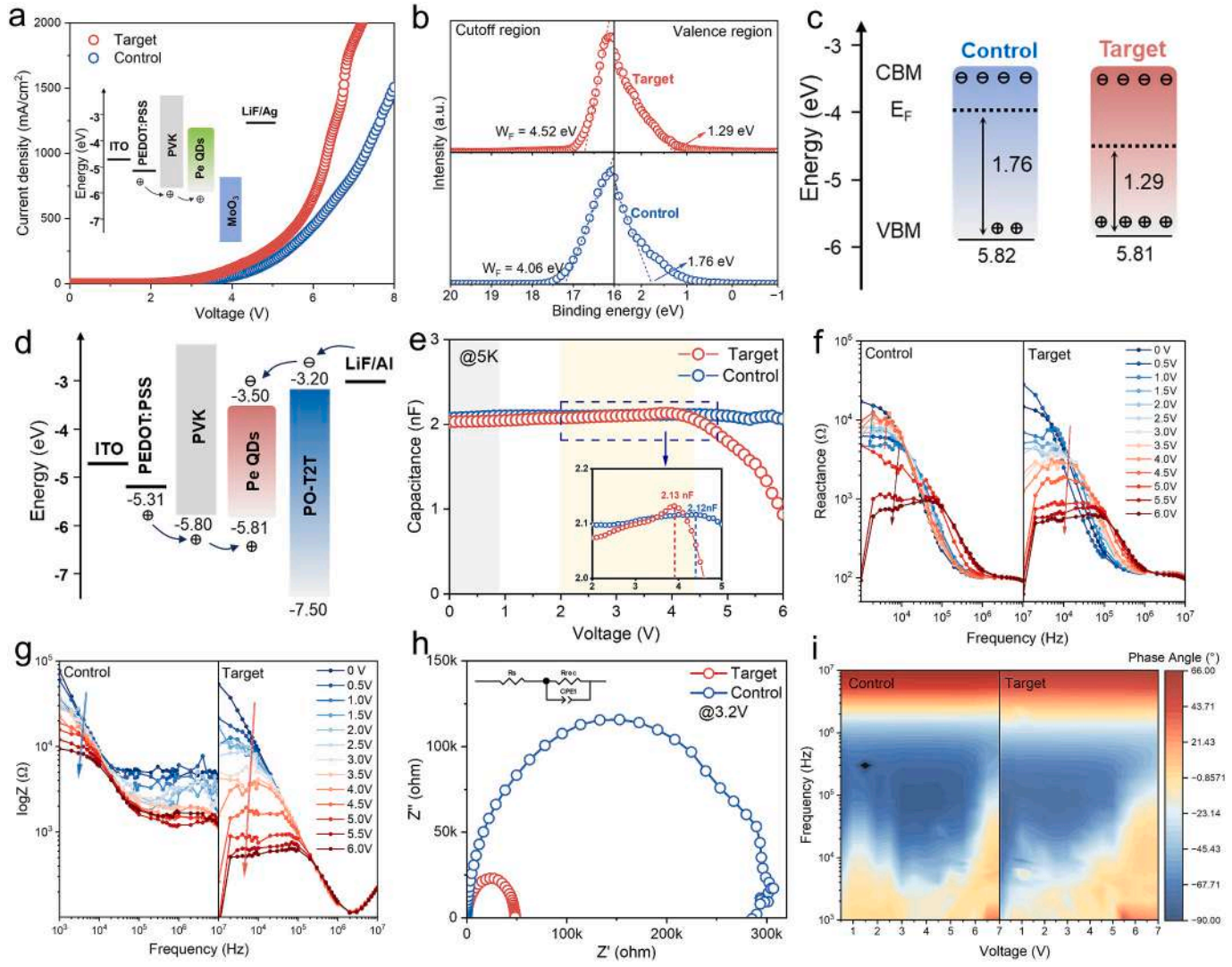


Fig. 3. Energy-level alignment and carrier dynamics in PeQLEDs. a) Current density-voltage diagram of hole-only devices. b) Ultraviolet photoelectron spectroscopy (UPS) spectra. c) Schematic energy-level diagrams of QD films. d) Schematic flat-band energy diagram. e) Low-frequency capacitance-voltage (*C*—*V*) curve measured at 5 K Hz. f) The reactance at different voltages. g) Impedance spectra under different bias voltages. h) Multiscale phase-angle response. i) Electrochemical impedance spectroscopy (EIS).

The μ_h increased from 2.40 × 10^{-5} cm^2 V^{-1} s^{-1} to 7.20 × 10^{-5} cm^2 V^{-1} s^{-1} with TrTPFB incorporation. The enhanced hole mobility can be attributed to reduced trap-assisted carrier scattering and improved film uniformity after TrTPFB modification.

Finally, the long-term stability of the TrTPFB-modified PeQDs was evaluated (Fig. 2h, i), the target film retained 96% of its initial PL intensity after seven days of storage in an ambient atmosphere at room temperature. In stark contrast, the PL intensity of the control film degraded significantly, maintaining only 53% of its original value over the same period. The rapid degradation of the control sample is attributed to the inherent ionic nature of the perovskite lattice and the labile desorption of native ligands [55]. In contrast, the robust chemical interactions between the TrTPFB molecules and the perovskite surface passivate surface defects, anchor the lattice structure, and suppress moisture-induced degradation. These results highlight that TrTPFB not only optimizes the optical properties but also enhances the structural integrity of the PeQDs, laying a solid foundation for the fabrication of high-performance and stable PeQLEDs.

To elucidate the origin of the enhanced charge-transport properties, current density-voltage (J-V) characteristics of hole-only devices were measured (Fig. 3a). The target device exhibits a significantly higher current density than the control, consistent with the reduced trap density and increased hole mobility established above SCLC analysis. Which is consistent with the enhanced hole current observed in the single-carrier devices Ultraviolet photoelectron spectroscopy (UPS) measurements were further conducted to investigate the electronic structure of the films (Fig. 3b-d). The Fermi level (E_F) of the control film was determined to be −4.06 eV, located relatively close to the conduction band minimum (CBM, approximately −3.5 eV), as derived from the bandgap spectra (**Fig. S12**). This energy-level alignment indicates that the control PeQDs exhibit relatively n-type electronic characteristics. After TrTPFB modification, the Fermi level shifts downward from −4.06 to −4.52 eV and moves closer to the valence band maximum (VBM), suggesting p-type electronic characteristics of the PeQD film [56–58]. Moreover, the VBM of the target PeQDs shifted upward to −5.81 eV, thereby reducing the hole-injection barrier at the PVK/PeQD interface. These energy-level shifts are consistent with the TrTPFB-induced surface charge redistribution revealed by the preceding DFT calculations. Specifically, the electron- withdrawing $TPFB^-$ anion promotes electron-density transfer from the PeQD surface, resulting in a p-type modulation effect, while the Tr^+ cation interacts with surface halides and stabilizes the local ionic environment [59]. Such electronic-structure regulation optimizes the energy-level alignment, suppresses interfacial charge accumulation, and facilitates more balanced carrier injection and recombination within the emissive layer. Importantly, the defect-passivation and charge-injection effects are closely coupled rather than independent processes. The reduced trap density minimizes trap-mediated carrier trapping and scattering, thereby improving carrier transport, whereas the favorable energy-level alignment lowers the hole-injection barrier. Their synergistic contribution alleviates interfacial charge accumulation and promotes balanced carrier recombination in PeQLEDs.

Capacitance–voltage (C—V) measurements were performed to investigate the influence of TrTPFB-modification on carrier injection and recombination in PeQLEDs. As shown in Fig. 3e, the target device exhibits a slightly higher diffusion capacitance (2.13 vs 2.12 nF) and a lower turn-on voltage (3.9 vs 4.4 V) in region 3, indicating enhanced carrier transport and reduced interfacial injection barriers. Moreover, a more pronounced capacitance decrease in region 4, which is associated with charge recombination, suggests improved carrier recombination efficiency. These results demonstrate that TrTPFB-induced p-type electronic modulation promotes charge injection and recombination while reducing interfacial charge accumulation. Consistent behavior is observed in the high-frequency C—V characteristics (**Fig. S13**). Under high-bias conditions, the lower high-frequency capacitance of the target device indicates enhanced charge recombination and reduced interfacial charge accumulation. Consistently, the reactance exhibits a voltage-dependent decrease. While the control device shows a rebound from 4715 Ω at 1.0 V to 9684 Ω at 4.5 V (10^3 Hz), indicative of charge accumulation and inefficient recombination, the target device displays a continuous decrease in reactance with increasing voltage, reflecting more efficient charge transport and reduced energy loss after TrTPFB-modification (Fig. 3f). A similar trend is observed in the impedance spectra (Fig. 3g), where the impedance of the target device decreases more rapidly, from 53,300 Ω at 0 V to 70 Ω at 6 V at 10^3 Hz. This result is consistent with the EIS measurements (Fig. 3h), which show a smaller semicircle radius for the target device, indicating reduced charge-transfer resistance [10,60]. Furthermore, the phase angle–frequency response (Fig. 3i) reveals pronounced oscillations in the control device, whereas the target device exhibits a monotonic decrease in phase angle with increasing bias below 3 × 10^5 Hz, suggesting more stable carrier transport and recombination processes. The reduced density of electrically active traps minimizes carrier trapping and scattering, whereas the TrTPFB-induced p-type electronic modulation lowers the hole-injection barrier and improves carrier balance. The combined optical and electrical evidence therefore establishes an experimental correlation between the local surface interactions identified by DFT and the device-scale charge dynamics.

To evaluate the effect of TrTPFB on device performance, $FAPbBr_3$ QLEDs with the structure ITO/PEDOT:PSS/PVK/PeQDs/PO-T2T/LiF/Al were fabricated (Fig. 4a). To investigate the concentration-dependent effect of TrTPFB, PeQLEDs containing different TrTPFB addition amounts of 3, 5, 8, and 10 mg were fabricated and characterized (**Fig. S14**). J–V–L and EQE measurements show that the device performance reaches its optimum at 5 mg and progressively deteriorates at higher loadings. The performance degradation at 8 and 10 mg suggests that excessive TrTPFB may weaken inter-dot electronic coupling and introduce local charge-transport barriers, thereby disturbing the balanced injection and recombination of electrons and holes and offsetting the beneficial effect of surface passivation. Therefore, 5 mg was selected as the optimal TrTPFB loading. Current density-voltage-luminance (J-V-L) characteristics of the corresponding devices are shown in Fig. 4b. The target device achieved a maximum luminance of 80,859.28 cd m^{-2}, substantially higher than that of the control device (22,245.15 cd m^{-2}). Besides, the target device displays a reduced turn-on voltage from 3.0 to 2.8 V. The higher luminance and lower turn-on voltage can be ascribed to suppressed nonradiative recombination loss of carriers and more efficient electron transport in the PeQLEDs with TrTPFB. The EL spectra remained centered at 528 nm without an observable peak shift, indicating stable and high-purity green emission (Fig. 4c**).** Meanwhile, the TrTPFB-based device shows stable EL spectra under incremental applied voltages (**Fig. S15**). Moreover, the peak external quantum efficiency (EQE) of the target device increased significantly from 9.20% to 17.50%, along with a huge improvement of the maximum current efficiency (CE) from 45.5 cd A^{-1} to 80.2 cd A^{-1} (Fig. 4d, e). The operational stability of the PeQLEDs was evaluated in a nitrogen atmosphere (Fig. 4f). The representative control and TrTPFB-modified devices exhibited maximum T_{50} lifetimes of 10.38 and 38.31 min, respectively. The average T_{50} lifetime increased from 7.84 ± 2.52 min for the control devices to 26.96 ± 8.74 min for the Target devices, corresponding to an approximately threefold enhancement. A two-tailed Welch's *t*-test yielded a *p* value of 0.0064, confirming that the improvement was statistically significant (**Fig. S16 and Table S5**). The improved operational stability can be attributed to the effects of surface-defect passivation, stabilization of the local ionic coordination environment, and mitigation of interfacial charge accumulation. These effects reduce trap-assisted nonradiative recombination and the local electric-field perturbations that may promote defection redistribution during device operation. Furthermore, statistical analysis of multiple device batches shows an average peak EQE of 14.61% for the target devices, compared with 9.03% for the control devices, demonstrating the high reproducibility and robustness of the TrTPFB-modification

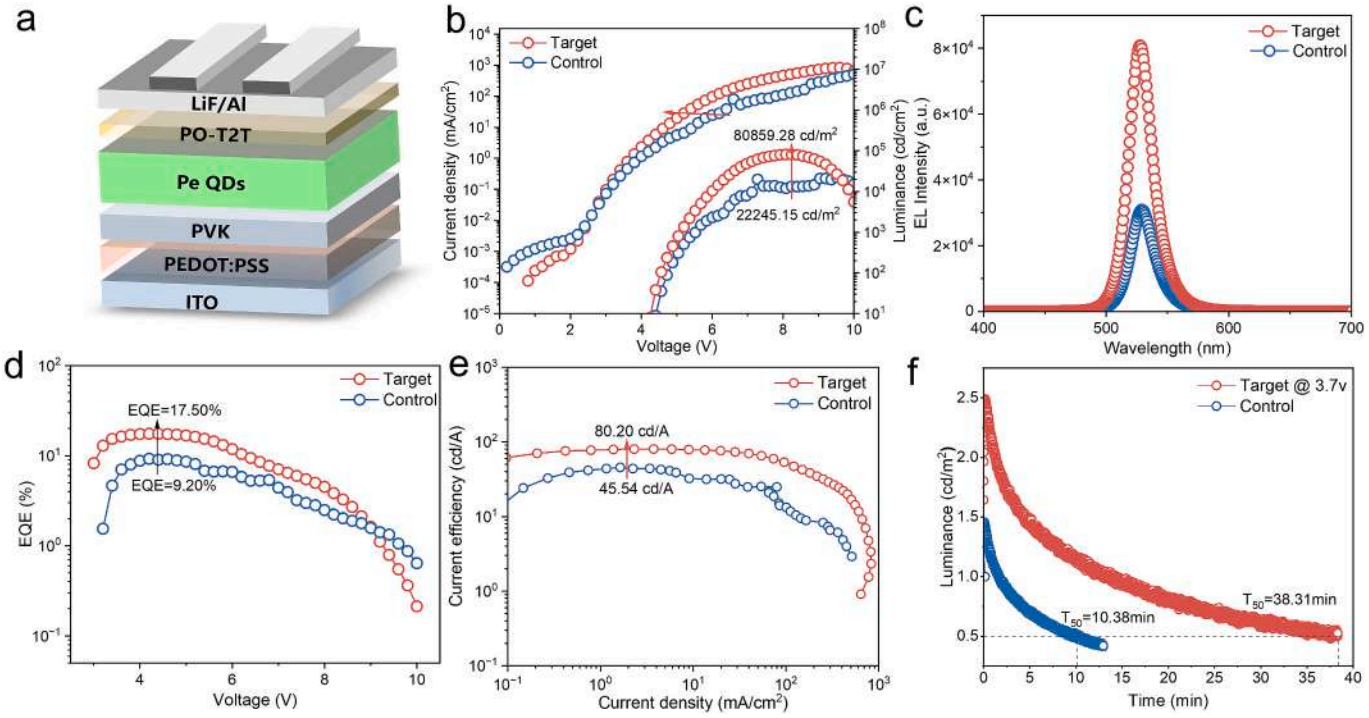


Fig. 4. Device architecture and electroluminescence performance of PeQLEDs. a) Schematic illustration of the PeQLED device structure. b) Current density-voltage-luminance (*J-V-L*) curves. c) Normalized electroluminescence (EL) spectra at 6.5 V. d) External quantum efficiency-voltage (*EQE-V*) curves. e) Current efficiency-current density (*CE-J)* curves. f) The operational lifetime under an initial luminance of ~100 cd m^{-2}.

strategy (**Fig. S17**). The electroluminescence performance and operational lifetime of selected representative green PeQLEDs are summarized in **Table S6.** Although our peak EQE is not the highest among the selected reports, the simultaneous realization of competitive efficiency, notably high luminance, and directly measured operational stability represents an important advantage of the present device. More importantly, the simultaneous improvements originate from a simple ionic-molecule strategy that integrates surface-defect passivation with charge-injection regulation.

3. Conclusion

In summary, we developed a fluorinated ionic molecular strategy by incorporating TrTPFB into $FAPbBr_3$ PeQDs to simultaneously regulate surface chemistry and charge-injection behavior. The $TPFB^-$ anion and Tr^+ cation interact with multiple ionic sites on the PeQD surface through F—Pb coordination, N-H···F hydrogen bonding, and electrostatic Tr^+-Br^- interaction, thereby stabilizing the surface coordination environment and suppressing trap-assisted nonradiative recombination. Meanwhile, the electron-withdrawing fluorinated groups induce p-type electronic modulation, improving hole injection and reducing interfacial charge accumulation. Benefiting from these synergistic effects, the optimized green PeQLED achieves a peak EQE of 17.50%, a maximum luminance of 80,859.28 cd m^{-2}, and an extended average T_{50} lifetime of 26.96 min, corresponding to an approximately threefold improvement over the control device. Compared with previous ligand-modification strategies that mainly optimize individual performance aspects, this work provides a simple and effective fluorinated ionic molecular strategy for coupling surface passivation with electronic regulation in efficient and stable PeQLEDs. Further studies combining spatially resolved ion-migration measurements with mesoscale multiphysics modeling may provide a quantitative description of defect redistribution and degradation during PeQLED operation.

4. Experimental section

4.1. Materials

Triphenylmethylium tetrakis(pentafluorophenyl)borate (TrTPFB, 98%), *N,N*-dimethylformamide (DMF, 99%), n-butanol (99%), n-hexane (99%), n-octane (99%), toluene (99.9%), oleic acid (OA, 90%), decylamine (98%) and chlorobenzene (99%) were purchased from Shanghai Aladdin Industrial Corporation Co., Ltd. Lead bromide ($PbBr_2$, 99.99%), formamidinium bromide (FABr, 99.5%), poly(3,4-ethylenedioxythiophene): polystyrene sulfonate (PEDOT:PSS, 1.5 wt% in water), poly(9-vinylcarbazole) (PVK), 2,4,6-Tris[3-(diphenylphosphinyl)phenyl]-1,3,5-triazine (PO-T2T, 99.5%), molybdenum trioxide (MoO_3, 99.95%), lithium fluoride (LiF, 99.9%), aluminum (Al, 99.99%) and silver (Ag, 99.99%) were obtained from Xi'an Yuri Solar Co., Ltd. All chemicals were used as received without further purification.

4.2. Synthesis of $FAPbBr_3$ quantum dots

$FAPbBr_3$ quantum dots (QDs) were synthesized via a modified ligand-assisted reprecipitation (LARP) method. A 0.2 M precursor solution was prepared by dissolving FABr and $PbBr_2$ in DMF at a molar ratio of 2.2:1. The crystallization-inducing solution consisted of toluene (5 mL), n-butanol (2 mL), oleic acid (500 μL), and decylamine (25 μL). For TrTPFB-modified QDs, 5 mg of TrTPFB was dissolved in the crystallization-inducing solution prior to precursor injection. The precursor solution was rapidly injected into the vigorously stirred crystallization-inducing solution and stirred for 10 min. The resulting suspension was centrifuged at 13,000 rpm for 5 min, and the precipitate was redispersed in a mixed solvent of n-octane and n-hexane. After a second centrifugation to remove aggregates, the supernatant containing monodisperse $FAPbBr_3$ QDs was collected for subsequent characterization and device fabrication.

4.3. Device fabrication

Patterned ITO substrates were cleaned by sequential ultrasonication in detergent, deionized water, acetone, isopropanol, and ethanol, followed by UV-ozone treatment for 30 min. PEDOT:PSS and PVK (6 mg/mL in chlorobenzene) were spin-coated at 4000 rpm for 40 s and annealed at 150 °C for 15 min and 160 °C for 20 min, respectively. The QD emissive layer was deposited by spin-coating the pristine or TrTPFB-modified QD solution at 1000 rpm for 30 s. Subsequently, PO-T2T (40 nm), LiF (1 nm), and Al (80 nm) were thermally evaporated under a vacuum of 8×10^{-5} Pa. Hole-only devices were fabricated with MoO_3 (3 nm)/Ag (90 nm) instead of PE PEDOT:PSS/PVK. The device area was 4 mm^2.The operational lifetime was measured under a constant bias voltage of 3.7 V, corresponding to an initial luminance of approximately 100 cd m^{-2}. The measurements were performed using unencapsulated devices in a nitrogen atmosphere. T_{50} was defined as the time required for the luminance to decrease to 50% of its initial value.

4.4. Characterization

SEM images were obtained using a JEOL JSM-7800 Prime microscope (5 kV). XRD patterns were recorded on an XPert Pro diffractometer with Cu Kα radiation (λ = 0.154 nm), and XPS spectra were collected using a Thermo Scientific ESCALAB 250Xi. UV–vis absorption spectra were measured with a Shimadzu UV-2500 spectrophotometer. The PL, TRPL, and temperature-dependent PL spectra were measured using an Edinburgh FLS980 spectrometer. The absolute PLQYs of the PeQD films were measured at room temperature using the same spectrometer equipped with an integrating sphere. The samples were excited at 365 nm, and the excitation-scattering and luminescence signals were integrated over 345–384 nm and 479–615 nm, respectively. The built-in Quantum Yield Wizard calculated the absolute PLQY according to $\Phi_{PL} = \frac{E_{sample} - E_{blank}}{S_{blank} - S_{sample}}$, where E and S denote the integrated luminescence and excitation-scattering signals, respectively [61]. No additional post-measurement self-absorption correction was applied; therefore, the reported values represent the directly measured absolute PLQYs [62]. Electrical characterizations, including C—V measurements, were performed using a Keithley 4200 parameter analyzer. Device performance was evaluated using a Keithley 2400 source meter and a QE-Pro spectrometer, and EL intensity was measured with a FOIS-1 integrating sphere.

4.5. Density functional theory (DFT)

All first-principles calculations were performed using the Vienna Ab initio Simulation Package (VASP). The Perdew-Burke-Ernzerhof (PBE) exchange-correlation functional was employed within the generalized gradient approximation (GGA). The Kohn-Sham wave functions were expanded in a plane-wave basis set with a kinetic energy cutoff of 450 eV. To simulate isolated species and surface interactions, models were constructed with a vacuum region exceeding 20 Å in the *X*, *Y*, and *Z* directions to minimize periodic image interactions. Brillouin zone integration was performed using a $1 \times 1 \times 1$ *Γ*-centered k-point mesh. The energy convergence criterion for the self-consistent field (SCF) cycles was set to 10^{-5} eV, utilizing a Gaussian smearing width of 0.05 eV. Furthermore, structural geometries were fully relaxed until the Hellmann-Feynman forces on each atom were less than 0.02 eV $Å^{-1}$. The interaction energies (E_{ads}) between the TrTPFB ionic species and the $FAPbBr_3$ QD surface.

Declaration of generative AI and AI-assisted technologies in the manuscript preparation process

During the preparation and revision of this work, the authors used OpenAI to assist with language refinement and to improve the readability and clarity of the manuscript. The tool was not used to generate experimental data, analyze results, interpret scientific findings, or draw scientific conclusions. After using this tool, the authors carefully reviewed and edited the content as needed and take full responsibility for the content of the published article.

All authors accept responsibility for the integrity, accuracy, and originality of the work.

CRediT authorship contribution statement

Di Shen: Writing – review & editing, Writing – original draft, Methodology, Investigation, Data curation. **Jianhao Ding:** Methodology, Investigation. **Yuhang Tan:** Investigation. **Yujie Wen:** Investigation. **Xinning Wang:** Investigation. **Xiankan Zeng:** Investigation, Data curation. **Maolin Mu:** Investigation. **Chenglong Li:** Investigation. **Jingjing Cao:** Project administration, Funding acquisition. **Xiaoqiang Fan:** Writing – review & editing. **Weiqing Yang:** Writing – review & editing, Data curation. **Wen Li:** Writing – review & editing, Supervision.

Originality and submission

This manuscript represents original work that has not been published previously and is not currently under consideration for publication elsewhere. If accepted, the manuscript will not be published elsewhere in the same form, in English or in any other language, including electronically, without the written consent of the copyright holder.

Authorship

All listed authors have made substantial contributions to the work, reviewed and approved the final version of the manuscript, and agreed to its submission to the Journal of Colloid and Interface Science.

Declaration of competing interest

The authors declare that they have no known competing financial interests or personal relationships that could have appeared to influence the work reported in this paper.

Acknowledgements

This work was financially supported by the National Key Research and Development Program Young Scientist Project (2023YFB3405700) and the National Natural Science Foundation of China (NSFC, grant no. 22509128). The authors would like to thank the Analysis and Testing Center of Southwest Jiaotong University for supporting the XRD and XPS measurements.

Appendix A. Supplementary data

Supplementary data to this article can be found online at https://doi.org/10.1016/j.jcis.2026.141247.

Data availability

Data will be made available on request.

References

[1] M.D. Smith, B.A. Connor, H.I. Karunadasa, Tuning the luminescence of layered halide perovskites, Chem. Rev. 119 (2019) 3104–3139, https://doi.org/10.1021/acs.chemrev.8b00477.
[2] H.-D. Lee, S.-J. Woo, S. Kim, J. Kim, H. Zhou, S.J. Han, K.Y. Jang, D.-H. Kim, J. Park, S. Yoo, T.-W. Lee, Valley-Centre tandem perovskite light-emitting diodes, Nat. Nanotechnol. 19 (2024) 624–631, https://doi.org/10.1038/s41565-023-01581-2.
[3] Y. Jiang, C. Sun, J. Xu, S. Li, M. Cui, X. Fu, Y. Liu, Y. Liu, H. Wan, K. Wei, T. Zhou, W. Zhang, Y. Yang, J. Yang, C. Qin, S. Gao, J. Pan, Y. Liu, S. Hoogland, E.

H. Sargent, J. Chen, M. Yuan, Synthesis-on-substrate of quantum dot solids, Nature 612 (2022) 679–684, https://doi.org/10.1038/s41586-022-05486-3.
[4] Z. Chen, Z. Li, C. Zhang, X.-F. Jiang, D. Chen, Q. Xue, M. Liu, S. Su, H.-L. Yip, Y. Cao, Recombination dynamics study on nanostructured perovskite light-emitting devices, Adv. Mater. 30 (2018) 1801370, https://doi.org/10.1002/adma.201801370.
[5] J. Zhang, B. Cai, X. Zhou, F. Yuan, C. Yin, H. Wang, H. Chen, X. Ji, X. Liang, C. Shen, Y. Wang, Z. Ma, J. Qing, Z. Shi, Z. Hu, L. Hou, H. Zeng, S. Bai, F. Gao, Ligand-induced cation–π interactions enable high-efficiency, bright, and spectrally stable rec. 2020 pure-red perovskite light-emitting diodes, Adv. Mater. 35 (2023) 2303938. doi:https://doi.org/10.1002/adma.202303938.
[6] S.-Q. Sun, J.-W. Tai, W. He, Y.-J. Yu, Z.-Q. Feng, Q. Sun, K.-N. Tong, K. Shi, B.-C. Liu, M. Zhu, G. Wei, J. Fan, Y.-M. Xie, L.-S. Liao, M.-K. Fung, Enhancing light outcoupling efficiency via anisotropic low refractive index electron transporting materials for efficient perovskite light-emitting diodes, Adv. Mater. 36 (2024) 2400421, https://doi.org/10.1002/adma.202400421.
[7] J.S. Kim, J.-M. Heo, G.-S. Park, S.-J. Woo, C. Cho, H.J. Yun, D.-H. Kim, J. Park, S.-C. Lee, S.-H. Park, E. Yoon, N.C. Greenham, T.-W. Lee, Ultra-bright, efficient and stable perovskite light-emitting diodes, Nature 611 (2022) 688–694, https://doi.org/10.1038/s41586-022-05304-w.
[8] M. Li, Y. Yang, Z. Kuang, C. Hao, S. Wang, F. Lu, Z. Liu, J. Liu, L. Zeng, Y. Cai, Y. Mao, J. Guo, H. Tian, G. Xing, Y. Cao, C. Ma, N. Wang, Q. Peng, L. Zhu, W. Huang, J. Wang, Acceleration of radiative recombination for efficient perovskite LEDs, Nature 630 (2024) 631–635, https://doi.org/10.1038/s41586-024-07460-7.
[9] Y. Miao, G. Sathiyan, H. Wang, X. Ding, M. Zhai, C. Yang, L. Liu, Z. Xia, C. Chen, M. Cheng, Enhancing the performance of perovskite solar cells through simple bilateral active site molecule assisted surface defect passivation, Chem. Eng. J. 432 (2022) 134223, https://doi.org/10.1016/j.cej.2021.134223.
[10] Y. Chen, C. Yan, Z. Chen, X. Zeng, Q. Wang, S. Yang, L. Pan, C. Li, M. Mu, W. Li, G. Tang, W. Yang, Interfacial coulomb-enhanced charge injection for efficient perovskite light-emitting diodes, Mater. Today Phys. 43 (2024) 101413, https://doi.org/10.1016/j.mtphys.2024.101413.
[11] Y. Wu, D. Chen, G. Zou, H. Liu, Z. Zhu, A.L. Rogach, H.-L. Yip, Strategies for stabilizing metal halide perovskite light-emitting diodes: bulk and surface reconstruction of perovskite nanocrystals, ACS Nano 19 (2025) 9740–9759, https://doi.org/10.1021/acsnano.5c00593.
[12] Z. Chen, Z. Li, T.R. Hopper, A.A. Bakulin, H.-L. Yip, Materials, photophysics and device engineering of perovskite light-emitting diodes, Rep. Prog. Phys. 84 (2021) 046401, https://doi.org/10.1088/1361-6633/abefba.
[13] Y. Bai, M. Hao, S. Ding, P. Chen, L. Wang, Surface chemistry engineering of perovskite quantum dots: strategies, applications, and perspectives, Adv. Mater. 34 (2022) 2105958, https://doi.org/10.1002/adma.202105958.
[14] Y. Li, X. Guan, Y. Zhao, Q. Zhang, X. Chen, S. Zhang, J. Lu, Z. Wei, Modulation of charge transport layer for perovskite light-emitting diodes, Adv. Mater. 37 (2025) 2410535, https://doi.org/10.1002/adma.202410535.
[15] L. Xu, G. Liu, H. Xiang, R. Wang, Q. Shan, S. Yuan, B. Cai, Z. Li, W. Li, S. Zhang, H. Zeng, Charge-carrier dynamics and regulation strategies in perovskite light-emitting diodes: from materials to devices, Appl. Phys. Rev. 9 (2022) 021308, https://doi.org/10.1063/5.0080087.
[16] K. Lin, J. Xing, L.N. Quan, F.P.G. De Arquer, X. Gong, J. Lu, L. Xie, W. Zhao, D. Zhang, C. Yan, W. Li, X. Liu, Y. Lu, J. Kirman, E.H. Sargent, Q. Xiong, Z. Wei, Perovskite light-emitting diodes with external quantum efficiency exceeding 20 per cent, Nature 562 (2018) 245–248, https://doi.org/10.1038/s41586-018-0575-3.
[17] L. Zhang, X. Yang, Q. Jiang, P. Wang, Z. Yin, X. Zhang, H. Tan, Y. (Michael) Yang, M. Wei, B.R. Sutherland, E.H. Sargent, J. You, Ultra-bright and highly efficient inorganic based perovskite light-emitting diodes, Nat. Commun. 8 (2017) 15640, https://doi.org/10.1038/ncomms15640.
[18] A. Fakharuddin, W. Qiu, G. Croes, A. Devižis, R. Gegevičius, A. Vakhnin, C. Rolin, J. Genoe, R. Gehlhaar, A. Kadashchuk, V. Gulbinas, P. Heremans, Reduced efficiency roll-off and improved stability of mixed 2D/3D perovskite light emitting diodes by balancing charge injection, Adv. Funct. Mater. 29 (2019) 1904101, https://doi.org/10.1002/adfm.201904101.
[19] M. Karlsson, Z. Yi, S. Reichert, X. Luo, W. Lin, Z. Zhang, C. Bao, R. Zhang, S. Bai, G. Zheng, P. Teng, L. Duan, Y. Lu, K. Zheng, T. Pullerits, C. Deibel, W. Xu, R. Friend, F. Gao, Mixed halide perovskites for spectrally stable and high-efficiency blue light-emitting diodes, Nat. Commun. 12 (2021) 361–370, https://doi.org/10.1038/s41467-020-20582-6.
[20] A. Vartanian, Ligands make a difference in perovskite light-emitting diodes, Nat. Rev. Mater. 8 (2023) 707, https://doi.org/10.1038/s41578-023-00613-6.
[21] W. Wang, L. Jing, Y. Zu, K. Yang, R. Gan, Y. Peng, D. Gong, P. Liu, X. Li, Z. Wu, A. Feng, Highly conductive ligands resurfacing perovskite quantum dots boost the efficiency of light-emitting diodes, JOL 292 (2026) 121755, https://doi.org/10.1016/j.jlumin.2026.121755.
[22] C. Shen, S. Fang, J. Zhang, X. Liang, C. Su, J. Qing, W. Cai, Y. Luo, R. Yang, L. Hou, High performance and stable pure-blue quasi-2D perovskite light-emitting diodes by multifunctional zwitterionic passivation engineering, Adv. Photonics 6 (2024) 026002, https://doi.org/10.1117/1.AP.6.2.026002.
[23] S. Mukherjee, A. Panigrahi, Y.-H. Lin, A. Perumal, Phosphine oxide based semiconducting small molecule as an additive and an electron transport layer enables efficient and stable perovskite light-emitting devices, J. Mater. Chem. C 12 (2024) 3365–3375, https://doi.org/10.1039/D3TC04461K.
[24] J. Chen, X. Liu, B. Cai, Y. Cheng, H. Wen, D. Zhu, Y. Xiong, L. Dai, X. Yan, B. Xiang, X. Luo, W. Feng, J. Du, S. Dong, Q. Shan, S. Chen, H. Zeng, Q. Xiong, L. Duan, D. Ma, Lattice-matched molecular-anchor design for high-performance perovskite quantum dot light-emitting diodes, Nat. Commun. 16 (2025) 8201, https://doi.org/10.1038/s41467-025-63684-9.
[25] R. Jayabalan, G.K. Hanumantharaju, T. Hettiger, A. Sarkar, F. Zu, A. Ullrich, A. Abfalterer, A.S. Urban, N. Koch, D. Andrienko, M. Scheele, W. Brütting, Optimizing carrier balance in CsPbBr3 nanocrystal LEDs: the role of alkyl ligands and polar electron transport layers, Adv. Opt. Mater. 13 (2025) e01361, https://doi.org/10.1002/adom.202501361.
[26] Y. Li, M. Deng, X. Zhang, L. Qian, C. Xiang, Proton-prompted ligand exchange to achieve high-efficiency $CsPbI_3$ quantum dot light-emitting diodes, Nano Micro Lett. 16 (2024) 105–114, https://doi.org/10.1007/s40820-024-01321-8.
[27] C. Zhao, C. Zhu, Z. Xu, Q. Ma, F. Yuan, J. Li, J. Xi, L. Li, S. Wang, B. Jiao, Z. Wu, Boosting carrier transport via functionalized short-chain conjugated ligands enables efficient green perovskite quantum dot light-emitting diodes, Chem. Eng. J. 501 (2024) 157596, https://doi.org/10.1016/j.cej.2024.157596.
[28] X. Wang, Y. Sun, J. Gao, X. Huang, D. Cao, X. Gao, H.-Y. Wang, Q. Li, Y. Wang, L.-M. Fu, X.-C. Ai, D. Xu, J.-P. Zhang, Overcoming the luminescence instability of colloidal mixed-halide perovskite quantum dots through ion motion confinement, J. Mater. Chem. C 12 (2024) 10487–10493, https://doi.org/10.1039/D4TC01279H.
[29] Y. Ji, Z. Chen, Y. Zhou, M. Wang, F. Xu, J. Shi, M.A. Padhiar, W. Zhang, X. He, K. An, L. Tong, L. Li, C. Sun, Reinforced mixed-halide lattice by dual-binding zwitterionic surface improvement for efficient perovskite nanocrystals LED, J. Alloys Compd. 1038 (2025) 182819, https://doi.org/10.1016/j.jallcom.2025.182819.
[30] C. Kirsch, T. Naujoks, P. Haizmann, P. Frech, H. Peisert, T. Chassé, W. Brütting, M. Scheele, Zwitterionic carbazole ligands enhance the stability and performance of perovskite nanocrystals in light-emitting diodes, ACS Appl. Mater. Interfaces 15 (2023) 32744–32752, https://doi.org/10.1021/acsami.3c05756.
[31] Y. Zhao, W. Feng, M. Li, J. Lu, X. Qin, K. Lin, J. Luo, W.-H. Zhang, E.L. Lim, Z. Wei, Efficient perovskite light-emitting diodes with chemically bonded contact and regulated charge behavior, Nano Lett. 23 (2023) 8560–8567, https://doi.org/10.1021/acs.nanolett.3c02335.
[32] Z. Chu, W. Zhang, J. Jiang, Z. Xia, M. Shi, B. Li, L. Dai, Y. Shen, Y. Li, N. C. Greenham, R.H. Friend, X. Zhang, J. You, Blue perovskite light-emitting diodes using multifunctional small molecule dopants, Adv. Mater. 37 (2025) 2409718, https://doi.org/10.1002/adma.202409718.
[33] H. Zhao, H. Chen, S. Bai, C. Kuang, X. Luo, P. Teng, C. Yin, P. Zeng, L. Hou, Y. Yang, L. Duan, F. Gao, M. Liu, High-brightness perovskite light-emitting diodes based on FAPbBr3 nanocrystals with rationally designed aromatic ligands, ACS Energy Lett. 6 (2021) 2395–2403, https://doi.org/10.1021/acsenergylett.1c00812.
[34] D.-H. Kim, S.-J. Woo, C.P. Huelmo, M.-H. Park, A.M. Schankler, Z. Dai, J.-M. Heo, S. Kim, G. Reuveni, S. Kang, J.S. Kim, H.J. Yun, J. Park, J. Park, O. Yaffe, A. M. Rappe, T.-W. Lee, Surface-binding molecular multipods strengthen the halide perovskite lattice and boost luminescence, Nat. Commun. 15 (2024) 6245, https://doi.org/10.1038/s41467-024-49751-7.
[35] Q. Wang, Y. Chen, C. Yan, X. Zeng, X. Fu, L. Pan, J. Cao, S. Yang, W. Li, X. Chen, W. Yang, Molecularly designing a passivation ETL to suppress EQE roll-off of PeLEDs, ACS Energy Lett. 8 (2023) 3710–3719, https://doi.org/10.1021/acsenergylett.3c01379.
[36] Y.-H. Kim, S. Kim, A. Kakekhani, J. Park, J. Park, Y.-H. Lee, H. Xu, S. Nagane, R. B. Wexler, D.-H. Kim, S.H. Jo, L. Martínez-Sarti, P. Tan, A. Sadhanala, G.-S. Park, Y.-W. Kim, B. Hu, H.J. Bolink, S. Yoo, R.H. Friend, A.M. Rappe, T.-W. Lee, Comprehensive defect suppression in perovskite nanocrystals for high-efficiency light-emitting diodes, Nat. Photonics 15 (2021) 148–155, https://doi.org/10.1038/s41566-020-00732-4.
[37] C. Wang, J. Xiang, J. Liu, C. Han, Z. Zheng, M. Xia, S. Shen, Z. Cui, X. Wang, J. Xie, X. Li, A. Mei, Y. Zhou, H. Han, Bifunctional compound induced dual back surface fields for efficient hole transport layer-free perovskite solar cells, Adv. Mater. (2025) 2502724, https://doi.org/10.1002/adma.202502724.
[38] X. Zhu, X. Luo, Y. Deng, H. Wei, Feng Peng, L. Ying, F. Huang, Y. Hu, Y. Jin, Doping bilayer hole-transport polymer strategy stabilizing solution-processed green quantum-dot light-emitting diodes, Sci. Adv. 10 (2024) eado0614, https://doi.org/10.1126/sciadv.ado0614.
[39] H. Huang, J. Raith, S.V. Kershaw, S. Kalytchuk, O. Tomanec, L. Jing, A.S. Susha, R. Zboril, A.L. Rogach, Growth mechanism of strongly emitting $CH_3NH_3PbBr_3$ perovskite nanocrystals with a tunable bandgap, Nat. Commun. 8 (2017) 996–1003. doi:https://doi.org/10.1038/s41467-017-00929-2.
[40] F. Zhang, M. Sun, X. Luo, D. Zhang, L. Duan, Modulation of ligand conjugation for efficient $FAPbBr_3$ based green light-emitting diodes, Mater. Chem. Front. 4 (2020) 1383–1389, https://doi.org/10.1039/C9QM00768G.
[41] I. Levchuk, A. Osvet, X. Tang, M. Brandl, J.D. Perea, F. Hoegl, G.J. Matt, R. Hock, M. Batentschuk, C.J. Brabec, Brightly luminescent and color-tunable formamidinium lead halide perovskite $FAPbX_3$ (X = cl, Br, I) colloidal nanocrystals, Nano Lett. 17 (2017) 2765–2770, https://doi.org/10.1021/acs.nanolett.6b04781.
[42] F. Urbach, The long-wavelength edge of photographic sensitivity and of the electronic absorption of solids, Phys. Rev. 92 (1953) 1324, https://doi.org/10.1103/PhysRev.92.1324.
[43] G. Li, J. Huang, H. Zhu, Y. Li, J.-X. Tang, Y. Jiang, Surface ligand engineering for near-unity quantum yield inorganic halide perovskite QDs and high-performance QLEDs, Chem. Mater. 30 (2018) 6099–6107, https://doi.org/10.1021/acs.chemmater.8b02544.
[44] A.D. Wright, C. Verdi, R.L. Milot, G.E. Eperon, M.A. Pérez-Osorio, H.J. Snaith, F. Giustino, M.B. Johnston, L.M. Herz, Electron–phonon coupling in hybrid lead

halide perovskites, Nat. Commun. 7 (2016) 11755, https://doi.org/10.1038/ncomms11755.
[45] T.J. Savenije, C.S. Ponseca, L. Kunneman, M. Abdellah, K. Zheng, Y. Tian, Q. Zhu, S.E. Canton, I.G. Scheblykin, T. Pullerits, A. Yartsev, V. Sundström, Thermally activated exciton dissociation and recombination control the carrier dynamics in organometal halide perovskite, J. Phys. Chem. Lett. 5 (2014) 2189–2194, https://doi.org/10.1021/jz500858a.
[46] J. Lee, E.S. Koteles, M.O. Vassell, Luminescence linewidths of excitons in GaAs quantum wells below 150 K, Phys. Rev. B 33 (1986) 5512–5516, https://doi.org/10.1103/PhysRevB.33.5512.
[47] R.L. Milot, G.E. Eperon, H.J. Snaith, M.B. Johnston, L.M. Herz, Temperature-dependent charge-carrier dynamics in CH_3 NH_3 PbI_3 perovskite thin films, Adv. Funct. Mater. 25 (2015) 6218–6227, https://doi.org/10.1002/adfm.201502340.
[48] A.K. Viswanath, J.I. Lee, D. Kim, C.R. Lee, J.Y. Leem, Exciton-phonon interactions, exciton binding energy, and their importance in the realization of room-temperature semiconductor lasers based on GaN, Phys. Rev. B 58 (1998) 16333–16339, https://doi.org/10.1103/PhysRevB.58.16333.
[49] B. Ai, C. Liu, Z. Deng, J. Wang, J. Han, X. Zhao, Low temperature photoluminescence properties of CsPbBr3 quantum dots embedded in glasses, Phys. Chem. Chem. Phys. 19 (2017) 17349–17355, https://doi.org/10.1039/C7CP02482G.
[50] J. Cui, A.P. Beyler, I. Coropceanu, L. Cleary, T.R. Avila, Y. Chen, J.M. Cordero, S. L. Heathcote, D.K. Harris, O. Chen, J. Cao, M.G. Bawendi, Evolution of the single-nanocrystal photoluminescence linewidth with size and shell: implications for exciton-phonon coupling and the optimization of spectral linewidths, Nano Lett. 16 (2016) 289–296, https://doi.org/10.1021/acs.nanolett.5b03790.
[51] K. Wei, M. Cui, C. Hu, S. Wei, Z. Zhang, T. Zhou, J. Zhang, X. Yue, K. Yin, C. Sun, S. Li, Y. Feng, S.M.H. Qaid, D. Zhao, X. Fu, W. Zhang, C. Qin, Y. Liu, Y. Jiang, M. Yuan, Managing edge states in reduced-dimensional perovskites for highly efficient deep-blue LEDs, Adv. Mater. 37 (2025) 2412041, https://doi.org/10.1002/adma.202412041.
[52] S. Wang, Y. Xie, W. Jiang, B. Liu, K. Shi, K. Pan, Incorporation sodium ions into monodisperse lead-free double perovskite $Cs_2AgBiCl_6$ nanocrystals to improve optical properties, Chin. Chem. Lett. 35 (2024) 108521, https://doi.org/10.1016/j.cclet.2023.108521.
[53] V.M. Le Corre, Space-charge-limited current measurements: a problematic technique for metal halide perovskites, J. Phys. Chem. Lett. 15 (2024) 10001–10008, https://doi.org/10.1021/acs.jpclett.4c02379.
[54] E.A. Duijnstee, J.M. Ball, V.M. Le Corre, L.J.A. Koster, H.J. Snaith, J. Lim, Toward understanding space-charge limited current measurements on metal halide perovskites, ACS Energy Lett. 5 (2020) 376–384, https://doi.org/10.1021/acsenergylett.9b02720.
[55] Y. Wu, Y. Liu, N. Fiuza-Maneiro, S. Gómez-Graña, M. Imran, L. Polavarapu, A. L. Rogach, X. Li, H. Zeng, Amine-free $CsPbBr_3$ perovskite nanoplatelets produced with monolayer-precision thickness control, ACS Mater. Lett. 6 (2024) 2425–2433, https://doi.org/10.1021/acsmaterialslett.4c00670.
[56] S. You, H. Zeng, Y. Liu, B. Han, M. Li, L. Li, X. Zheng, R. Guo, L. Luo, Z. Li, C. Zhang, R. Liu, Y. Zhao, S. Zhang, Q. Peng, T. Wang, Q. Chen, F.T. Eickemeyer, B. Carlsen, S.M. Zakeeruddin, L. Mai, Y. Rong, M. Grätzel, X. Li, Radical polymeric p-doping and grain modulation for stable, efficient perovskite solar modules, Science 379 (2023) 288–294, https://doi.org/10.1126/science.add8786.
[57] W. Xiong, W. Tang, G. Zhang, Y. Yang, Y. Fan, K. Zhou, C. Zou, B. Zhao, D. Di, Controllable p- and n-type behaviours in emissive perovskite semiconductors, Nature 633 (2024) 344–350, https://doi.org/10.1038/s41586-024-07792-4.
[58] H. Cui, W. Chen, X. Yang, S. Zhou, C. Wang, G. Chen, S. Du, K. Dong, S. Wang, H. Fu, W. Wang, W. Ke, G. Fang, Grains $>$ 2 μ m with regulating grain boundaries for efficient wide-bandgap perovskite and all-perovskite tandem solar cells, Adv. Mater. 37 (2025) 2502770. doi:https://doi.org/10.1002/adma.202502770.
[59] H. Wang, Y. Dou, P. Shen, L. Kong, H. Yuan, Y. Luo, X. Zhang, X. Yang, Molecule-induced p-doping in perovskite nanocrystals enables efficient color-saturated red light-emitting diodes, Small 16 (2020) 2001062, https://doi.org/10.1002/smll.202001062.
[60] Y. Feng, J. Bian, S. Wang, C. Zhang, M. Wang, Y. Shi, Soft interfaces within hybrid perovskite solar cells: real-time dynamic tracking of interfacial electrical property evolution by EIS, J. Mater. Chem. C 7 (2019) 8294–8302, https://doi.org/10.1039/C9TC01770D.
[61] J.C. de Mello, H.F. Wittmann, R.H. Friend, An improved experimental determination of external photoluminescence quantum efficiency, Adv. Mater. 9 (1997) 230–232, https://doi.org/10.1002/adma.19970090308.
[62] T.-S. Ahn, R.O. Al-Kaysi, A.M. Müller, K.M. Wentz, C.J. Bardeen, Self-absorption correction for solid-state photoluminescence quantum yields obtained from integrating-sphere measurements, Rev. Sci. Instrum. 78 (2007) 086105, https://doi.org/10.1063/1.2768926.